[UCI]I804:21031-200000333364

Thesis for the Degree of Master Engineering

Bulk Heterojunction Solar Cells based on modified-Polyethylenimine Ethoxylated Cathode Interfacial Layers

by Adi Prasetio

Department of Display Science and Engineering

Graduate School of Engineering

Pukyong National University

2020.8

Bulk Heterojunction Solar Cells based on modified-Polyethylenimine Ethoxylated Cathode Interfacial Layers

(수정된-Polyethylenimine Ethoxylated 음극 계면층을 기반으로 한 벌크 이종접합 태양전지)

Advisor:

Prof. Yong Hyun Kim

by

Adi Prasetio

A thesis submitted in partial fulfillment of the requirements for the degree of

Master Engineering

in Department of Display Science and Engineering

Graduate School of Engineering

Pukyong National University

2020.8

Bulk Heterojunction Solar Cells based on modified-Polyethylenimine Ethoxylated Cathode Interfacial Layers

A thesis

by

Adi Prasetio

Approved by:

……....

Prof. Kwon-Taek Lim (위원장명)

……...……

Prof. Yeon-Tae Jeong (위원명)

…….....…

Prof. Yong Hyun Kim (위원명)

2020.8.28

Contents

List of Figures

List of Tables

Bulk Heterojunction Solar Cells based on modified-Polyethylenimine Ethoxylated Cathode Interfacial Layers

Adi Prasetio

Department of Display Science and Engineering, The Graduate School

Pukyong National University

Abstract

A low-cost polyelectrolyte, Polyethylenimine 80% ethoxylated (PEIE) has been widely used as an interface modified layer in flexible organic light-emitting diodes and organic solar cells. However, the PEIE has lower charge transfer compare to metal oxides. In this study, the device performance of bulk heterojunction solar cells is remarkably improved by modifying the PEIE using a hydrophobic molecule stearic acid. As a result, the stearic acid-modified-PEIE (denoted as m-PEIE) device achieved an improved power conversion efficiency (PCE) of 9.84% (FF 0.67, J_{SC} 18.78 mA cm^{-2}, V_{OC} 0.79 V) for the rigid device and 8.39% (FF 0.66, J_{SC} 16.65 mA cm^{-2}, V_{OC} 0.78 V) for the flexible device. Meanwhile, the PEIE pristine device only obtained a PCE of 8.45% (FF 0.62, J_{SC} 17.55 mA cm^{-2}, V_{OC} 0.77 V) for rigid and 7.55% (FF 0.64, J_{SC} 15.53 mA cm^{-2}, V_{OC} 0.76 V) for the flexible device. The ZnO device achieved a PCE of 9.02% for rigid and noticeably decreased on a flexible device which only shows a PCE of 5.32%. Furthermore, the long-term air–storage stability is substantially improved (87.75% retention after 10 days) which is superior to PEIE pristine device. These improvements in device stability and the photovoltaic performance are attributed to the

increase of hydrophobicity of the cathode interfacial layers (CILs). Atomic force microscopy (AFM) characterization shows that m-PEIE based device has more smooth roughness which facilitates better charge transfer at the cathode/photoactive layer interface. Moreover, the m-PEIE device has less charge recombination compared to PEIE device according to the light intensity-dependent, dark J-V, and electrochemical impedance spectroscopy (EIS) analysis. Besides, the m-PEIE device has better stability in ambient conditions due to its hydrophobic long hydrocarbon chain of stearic acid which protects the device from moisture. The m-PEIE based device retained over 87% of the initial efficiency after 10 days. More importantly, the m-PEIE layer does not require a further thermal annealing treatment which is beneficial for flexible devices.

Keywords: Bulk-heterojunction, solar cell, polyethylenenimine ethoxylated, cathode interfacial layer

수정된-Polyethylenimine Ethoxylated 음극 계면층을 기반으로 한 벌크 이종접합 태양전지

Adi Prasetio

부경대학교 대학원 융합디스플레이공학과

요약

저비용 고분자 전해질 polyethylenenimine 80 % ethoxylated (PEIE)는 유연한 유기 발광 다이오드 및 유기 태양 전지의 계면 개질 층으로서 널리 사용되어왔다. 그러나, PEIE 는 금속 산화물에 비해 전하 이동이 더 낮다. 이 연구에서, 벌크 이종접합 태양 전지의 소자 성능은 소수성 분자 스테아르 산을 사용하여 PEIE 를 변형시킴으로써 현저하게 개선된다. 그 결과, stearic-acid 변성 PEIE (m-PEIE 로) 장치는 강성 장치에 대해 9.84 % (FF 0.67, J_{SC} 18.78 mA cm^{-2}, V_{OC} 0.79 V)의 향상된 전력 변환 효율 (PCE)을 달성했습니다. 플렉서블 디바이스의 경우 8.39 % (FF 0.66, J_{SC} 16.65 mA cm^{-2}, V_{OC} 0.78 V). 한편 PEIE pristine 장치는 PCE 는 8.45 % (FF 0.62, J_{SC} 17.55 mA cm^{-2}, V_{OC} 0.77 V), 7.55 % (FF 0.64, J_{SC} 15.53 mA cm^{-2}, V_{OC} 0.76 V)에 불과했습니다. ZnO 장치는 PCE 가 9.02 %로 딱딱하고 PCE 는 5.32 % 만 보이는 유연한 장치에서 눈에 띄게 감소했습니다. 또한, 장기 공기 저장 안정성이 실질적으로 개선되어 (10 일 후 보유율 87.75 %) PEIE 깨끗한 장치보다 우수합니다. 소자 안정성 및 광기 전 성능에서의 이러한 개선은 cathode interfacial layer (CIL)의 소수성의 증가에 기인한다. Atomic force microscopy

(AFM) 특성화는 m-PEIE 기반 장치가 캐소드 / 광활성 층 계면에서 더 나은 전하 전달을 용이하게하는보다 부드러운 거칠기를 갖는다는 것을 보여준다. 또한, m-PEIE 소자는 광도 의존, 암색 J-V 및 electrochemical impedance spectroscopy (EIS) 분석에 따라 PEIE 소자에 비해 전하 재결합이 적다. 또한, m-PEIE 장치는 장치를 습기로부터 보호하는 스테아르 산의 소수성 장 탄화수소 사슬로 인해 주변 조건에서 더 우수한 안정성을 갖는다. m-PEIE 기반 장치는 10 일 후에도 초기 효율의 87 % 이상을 유지했습니다. 더 중요한 것은, m-PEIE 층은 유연한 장치에 유리한 추가적인 열 어닐링 처리를 필요로하지 않는다.

키워드: 벌크 이종접합, 태양전지, polyethylenenimine ethoxylated, 음극 계면층

Chapter 1 Introduction

1.1 Motivation

Global energy consumption and CO_2 emissions steadily rise which affects environmental, geopolitical and economic problems. The two-thirds of the total energy is produced from fossil fuels such as oil, coal and natural gas. However, due to the shortage of these natural resources and the rising of the pollution, renewable, and 'green' energy is urgently needed to be developed to tackle these problems. Today, the use of photovoltaic (PV) only 2% of total energy consumption. Nonetheless, the use of solar energy in 2040 is predicted to be about 18%. We can observe in **Figure 1.1** that PV promises the enormous potential to fulfill energy consumption.[1]

Typically, PV technologies are divided into three generations. The first generation such as monocrystalline and polycrystalline silicon PVs have high power conversion efficiency (PCE). However, these PVs have high manufacturing costs. The second generation is thin-film PVs such as copper indium selenide (CIS), cadmium telluride (CdTe) and copper indium gallium diselenide (CIGS) PVs. Nonetheless, these PVs have tellurium and indium which are very rare materials in nature. The last one, the third generation PVs are copper zinc tin sulfide (CZTS), perovskite solar cells (PSCs), dye-sensitized solar cells (DSSCs), quantum dot

solar cells (QDSCs) and organic solar cells (OSCs). Most of these PVs are solution-processed from semiconductor solutions.[2]

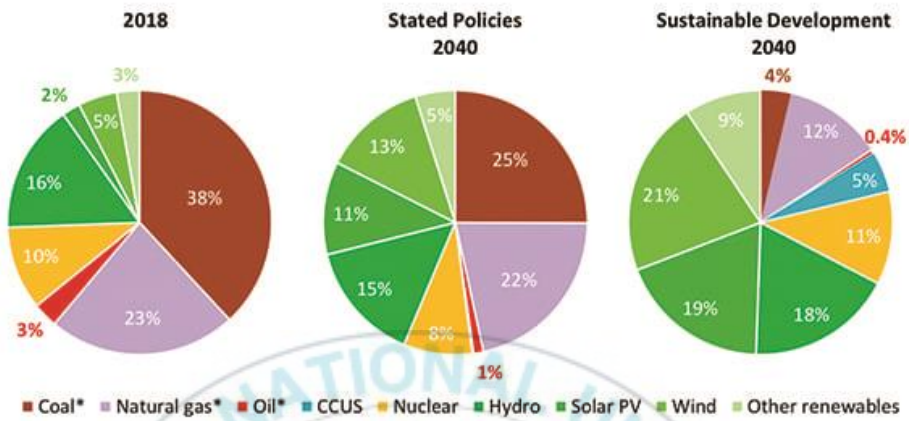

Figure 1.1 Global electricity generation in 2018, IEA's stated policies and sustainable development scenario.[1]

From the NREL efficiency chart (**Figure 1.2**), we can see that organic photovoltaic (OPV) is an emerging solar cell with a high increase in efficiency of 17.4%.[3] Moreover, the OPV is one of the most promising PV due to its high PCE, easy-processed using roll-to-roll coating, high-flexibility, and tunable band-gap for low-light indoor and semitransparent applications. The tunable light absorption in different colors makes OPV become the most suitable for building-integrated PV market. Besides, the flexibility of the OPV becomes an advantage compared to rigid PVs for a wide range of applications such as the roof of houses that cannot handle the heavy rigid PVs, clothes, roofs of cars and others.[4,5]

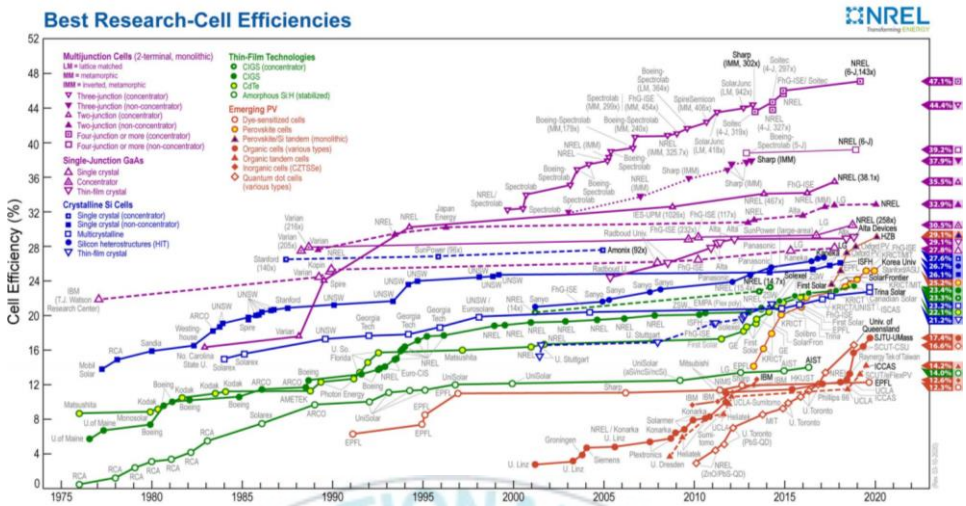

Figure 1.2 NREL efficiency chart 2020.

Commonly, for the inverted OPV, the polyethylene naphthalate (PEN) and polyethylene terephthalate (PET) were used as substrates. However, these substrates become unstable when heated over than 120°C for PEN and 78°C for PET.[6] Moreover, the performance of flexible devices, particularly those with inverted structures lag behind compared to rigid devices due to the rigidity of electron transport layers (ETLs) laying on metal oxide semiconductors (ZnO, SnO_2 and TiO_2).[7–11]

Polyethylenimine ethoxylated (PEIE) is a strong candidate polyelectrolyte for flexible OPV because it could exhibit good exhibit flexibility and device efficiency when fabricated without annealing treatment.[12,13] Different form metal oxide layer, PEIE work as a cathode interfacial layer (CILs) instead of ETL. The aliphatic amine groups of PEIE lower the work function of ITO by aligning the

permanent dipole. The WF of the ITO has play-role for efficient charge extraction. Nonetheless, the non-conjugated nature of PEIE weakens charge extraction due to its electrical insulating behavior and the hydrophilic tail of PEIE worsens the long-term device stability.[11,13]

Herein we demonstrated the hydrophobic modification of PEIE (denoted as m-PEIE) using a stearic acid molecule, a polyunsaturated fatty acid which is practically a very hydrophobic material and insoluble in water. The m-PEIE exhibits excellent charge transport and good long-term device stability which is superior to those of PEIE CIL. The *m*-PEIE CIL exhibit properties that surpass those of PEIE CIL. Specifically, (1) the interfacial charge transport and the ambient stability was significantly enhanced; (2) for the flexible device, the device stability during bending was improved. The *m*-PEIE ETLs achieved a PCE of 9.84% (J_{SC} of 18.78 mA cm^{-2}, FF of 0.67 and V_{OC} of 0.79 V), whereas the PEIE shows a poor PCE of 8.43% (J_{SC} of 17.66 mA cm^{-2}, FF of 0.62 and V_{OC} of 0.77 V). The m-PEIE flexible device achieved a PCE of 8.60% with a V_{OC} of 0.76 V, J_{SC} of 16.89 mA cm^{-2}, and a FF of 0.67 which is superior to those of PEIE flexible device with a PCE of 7.55% (a V_{OC} of 0.76 V, J_{SC} of 15.53 mA cm^{-2}, and a FF of 0.64). For comparison, the ZnO flexible device only achieved a PCE of 5.32%. The mechanical and air-storage stability was also simultaneously improved by introducing the stearic acid to the PEIE.

Chapter 2 Background

2.1. Bulk Heterojunction (BHJ) Solar Cells

The organic photovoltaic (OPV) with bulk heterojunction (BHJ) structures are made from a solid-state mixture of donor and acceptor molecules with nanostructured morphology. Conjugated polymers, oligomers or conjugated pigments are usually employed as the donor, and the fullerene or non-fullerene derivatives are used for the acceptor. These donor and acceptor molecules are self-assembling to form bi-continuous interpenetrating networks.[14,15]

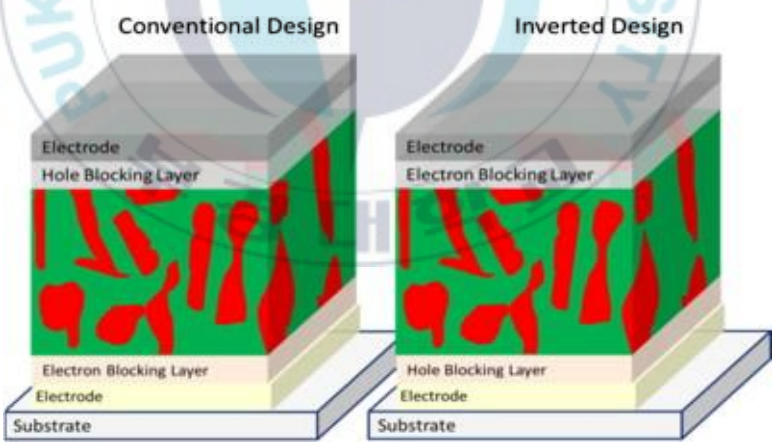

Figure 2.1 The scheme of the conventional and inverted structure of bulk heterojunction solar cells.[16]

The higher efficiency of BHJ cells comparing to D-A bilayer cells can be associated with the reduction of exciton losses owing to a larger D-A interfacial area and the reduced the dimensions of donor and acceptor domain where the excitons are formed and must diffuse to reach the D-A interface. If the length of the D-A blend is close to the donor and acceptor diffusion lengths (~10 nm length scale), most of the excitons will reach the heterojunction interface allowing to increase the active layer thickness. One of the most possible limiting factors to the performance of BHJ cells is the non-geminate recombination process.[15–17] This recombination occurs when the electrons and holes dissociated from the different excitons recombine. However, in recent years, the overall efficiency of BHJ cells rapidly increases, >10% for fullerene-based and >16% for non-fullerene-based devices.[18,19]

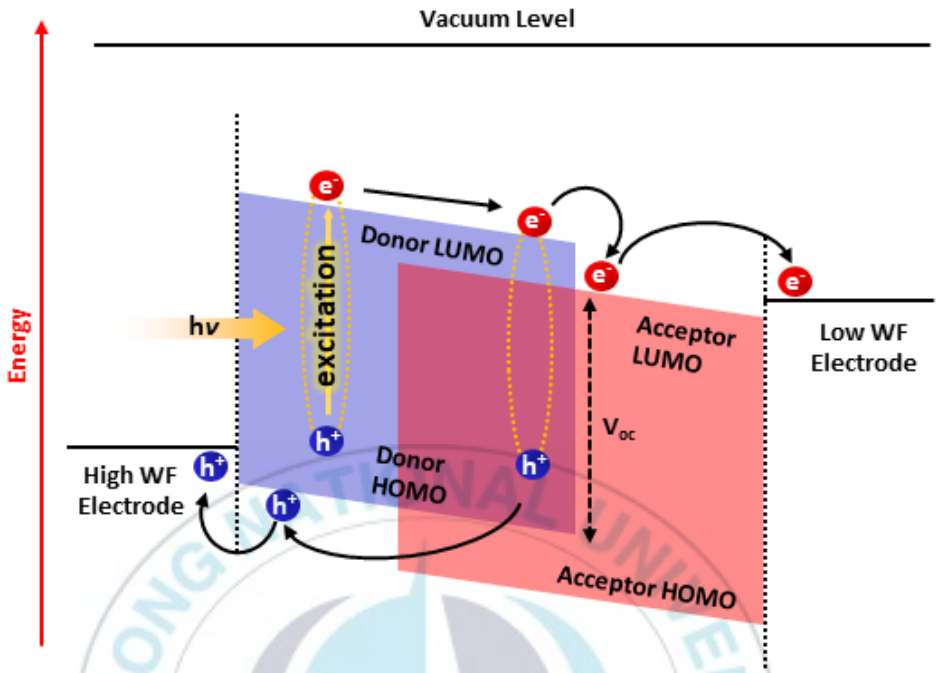

Figure 2.2 The working principles of a bulk heterojunction (BHJ) solar cell.

In BHJ cells, there are five processes are required to convert the absorption of incident light into electrical power: exciton formation via the absorption of photons by the active materials, exciton diffusion into the D-A interface, photo-induced charge separation of excitons into electrons and holes, charge transport through donor phase for holes and acceptor phase for electrons to the interface of electrodes, and the collection of electrons by the cathode and holes by the anode as shown in **Figure 2.2**.[20]

The absorbed light in the active layer promotes electrons in the ground state to an excited state. An excited state can be assumed as a quasi-particle (exciton). This exciton might be transferred to a neighboring molecule. Under ambient conditions, a dissociation of the exciton into free carriers is not likely to happen because of a strong Coulomb attraction between the electron and the hole. The dissociation of the excitons into free carriers can only happen if the driving force is sufficient enough to overcome the Coulomb energy (E_B) between the electron-hole pair.

Light absorption typically involves the D-A blend layer and the strongest absorption is mostly in the donor phase. The efficiency of the light absorption is depending on the optical absorption coefficient of donor and acceptor which is associated with density, molar extinction coefficient, the absorption cross-section. The absorption coefficient is limited by the difference between HOMO and LUMO levels in that manner that only photon with energy higher than the energy gap (E_g) can be absorbed. However, the absorption coefficient in organic materials is much higher than Si in such a way, basically with ~100 nm thickness of the active layer is enough to absorb 60-90% of the absorbed light. The absorption efficiency is also influenced by the light pathway length inside the active layer which

depends on the film thickness. The light pathway inside the active layer is influenced by reflection, refraction, and scattering at the interfaces between layers inside the device and at the device/air interface. The other factor that influences the light absorption efficiency is the cross-section of the active layer absorption with the solar spectrum Air Mass (AM) 1.5.[15,20,21]

For the exciton separation into free carriers, the exciton should diffuse to the D-A interface dissociation sites. Typically, exciton formed in the donor phase diffuses to the D-A interface as long as the geminate recombination does not occur. To successfully compete with various recombination, the donor domain size in the D-A blend should be controlled approximately in the same length with the exciton diffusion length (10 – 20 nm). The exciton diffused to the D-A interface is favorable dissociate if the energy difference between ionization potential of the electron-donating material and the electron affinity is higher than the exciton binding energy. The ultrafast charge transfer at the D-A interface is typically occurred immediately (~50 fs) after photoexcitation. However, the hole stays on the donor domains and the electron is transferred into the electron domains. By introducing an electric built-in field, these carriers might be swept-out to the corresponding electrode to generate photocurrent. The internal electric field

can be built by using two electrodes with different work functions. Nonetheless, if the difference is too small, the geminate recombination likely occurs.[15,20]

The charge transport in organic semiconductors relies on the order degree of molecular species. In an organic semiconductor, which is typically amorphous or semi-crystalline, the conductive electronic states are localized. The charges are localized on a single molecule and polarize forming the polaron. The charge carrier transport occurs via hopping transport mechanism between adjacent molecules. This mechanism is less efficient and is responsible for low charge mobility (<10-2 $cm^2 V^{-1}s^{-1}$).[20–22]

For the charge collection at the electrodes, the work-function of the cathode should be lower than the acceptor LUMO level and the work-function of anode should be higher than the donor HOMO level. These energy levels are responsible for the Ohmic or blocking contact for the charge extraction at corresponding electrodes. If the Ohmic contact is formed, the charge will be efficiently collected so that higher efficiency can be achieved otherwise the charge cannot be collected efficiently due to the energy barrier. The selectivity of the electrode should be carefully considered to minimize the non-geminate recombination because of the non-

selective charge extraction at the active layer/electrode interface. To date, the buffer layer is usually placed in between. This buffer layer will be explained in detail in the next sub-chapter.[15,20,22,23]

2.2. Cathode Interfacial Layer

The cathode interfacial layer (CIL) has a key role to facilitate the transfer of the electrons into the cathode. In an inverted structure, the CIL should have the following properties: i) it should be transparent and stable, ii) it has to efficiently transport electrons and block holes, and iii) it has to form an Ohmic contact with an acceptor material.[24]

Depending on its mechanism, the CIL is classified into two main groups as shown in **Figure 2.3**. The first one is the electron transport layer (ETL), which modulates the Fermi level (E_F) of the cathode with their energy levels and form intermediate energy states to facilitate charge transport. The doped semiconductors such as metal oxides and conducting polymers are mainly used for this kind of CIL. The metal oxides such as TiO_x and ZnO respectively possess wide band-gap 3.7 and 3.37 eV also act as the exciton blocking layers lead to better R_{SH}. Moreover, these metal oxides also serve as the spacer which locates the photoactive layer at the

maximum optical field resulting in better light absorption. Nonetheless, even after the E_F alignment, the additional energy barrier is formed between ETL and cathode due to a mismatch between the EF of the cathode and the energy bands (valence and conduction band) of the ETL. Moreover, because of the integer charge transfer states, the E_F pinning likely occurs at the ETL/organic semiconductor interface.[24]

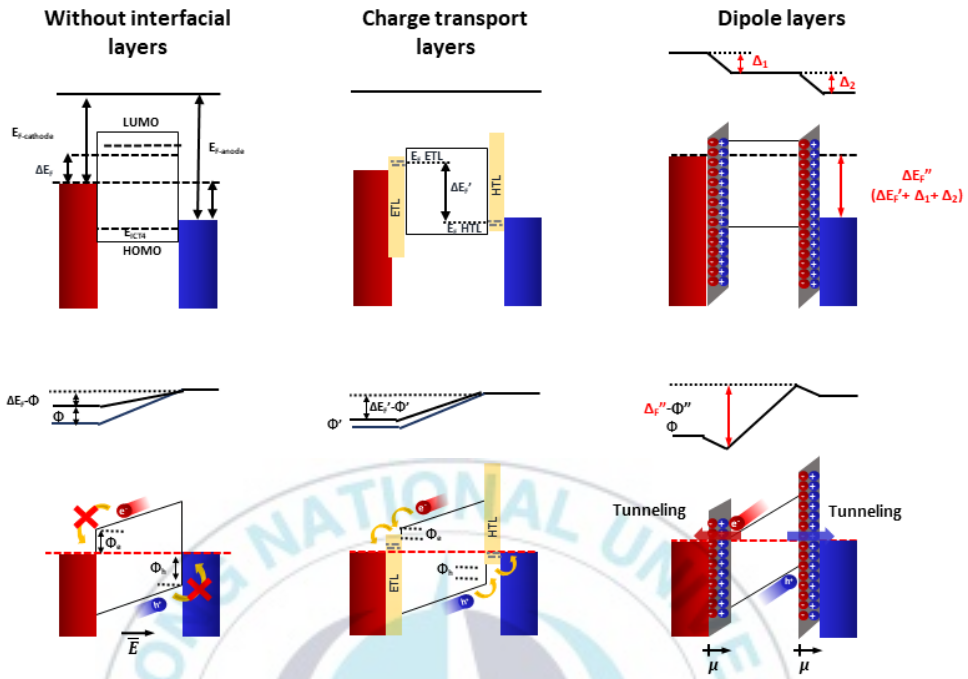

Figure 2.3 Diagram schematic of the working principle for OPV device without interfacial layers, with charge transport layers and dipole layers.

The other group is the electron dipole layer (EDL) which forms dipole energy at the photoactive/cathode interface. The EDL shifts the vacuum energy level and allows the electron for tunneling. Moreover, the charge selectivity induced by the developed electric potential distribution at the cathode/photoactive layer interface is improved, and it leads to lower surface recombination. The EDL materials are typically conjugated

polyelectrolytes (CPEs) such as WPF-oxy-F and PFN and non-conjugated polyelectrolytes such as PAA, PEI, and PEIE. [8,13,24]

2.3. Photocurrent Density – Voltage (J-V) Curves

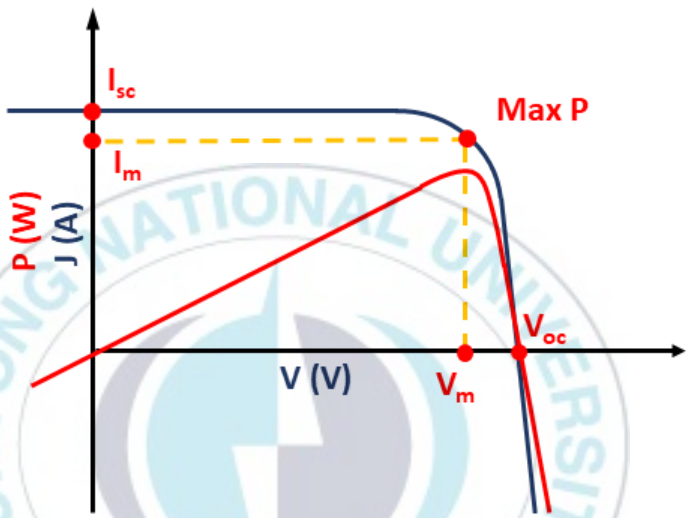

Figure 2.4 The photocurrent density-voltage (J-V) characteristics of a photovoltaic device.

The open-circuit voltage (V_{OC}), the short-circuit current density (J_{SC}), the fill factor (FF) and the power conversion efficiency (PCE) are the most important parameters of a photovoltaic device can be derived from J-V curves.

The V_{OC} is the maximum voltage when there are no current flows (J=0). The difference between the donor highest occupied molecular orbital (HOMO) and the acceptor lowest unoccupied molecular orbital (LUMO) determines the open-circuit voltage (V_{OC}) and determined by **Equation 2.1**:

$$\boldsymbol{V_{OC} \approx Edonor(HOMO) + Eacceptor(LUMO) + \frac{kB}{e\{(\ln(\frac{ne\,nh}{Nc^2})\}}} \qquad \textbf{(2.1)}$$

the electron and hole densities are respectively noted as n_e and n_h. The corresponding density of states (DOS) near the donor HOMO and the acceptor LUMO is noted as N_c. The V_{OC} can be increased by the difference between in work function of the cathode and anode. Moreover, the interface layer (electron or hole transport layer) or dipole layer can also improve the V_{OC} by modifying the cathode or anode work function.[15]

The J_{SC} is the current flowing when there is no external field applied (V=0). It is mainly determined by the number of photoexcitation depending on the absorption coefficient and band-gap of the donor materials. The other factors are the quantum efficiency and the transport of the charge carriers through solar cells. These factors strongly depend on the carriers' mobility

in both donor and acceptor phases and the interfaces between layers in solar cells.[15,20]

Theoretically, the FF is the proportion of the small square determined by J_{max} and V_{max} to the large square determined by J_{SC} and V_{OC} as shown in **Figure 2.4**. The FF indicates the quality of the cell showing the competition between recombination and the photogenerated carriers swept-out by the external field. In mathematical terms, the FF is shown in **Equation 2.2.**

$$\boldsymbol{FF = \frac{P_{max}}{I_{SC} \cdot V_{OC}}} \qquad \textbf{(2.2)}$$

where the P_{max} is the maximum electrical power generated by the cells under light illumination and is corresponding to the maximum power point (MPP). From this MPP, the I_{max} and V_{max} can be defined. The ratio between P_{max} and the incident light irradiance (P_{in}) defines the power conversion efficiency (PCE). The PCE, frequently denoted as η, is the proportion of the power output (P_{out}) to P_{in} (100 mW cm^{-2}) as shown in **Equation 2.3.**

$$\boldsymbol{PCE\ (\eta) = \frac{P_{out}}{P_{in}} = \frac{J_{SC} \cdot V_{OC} \cdot FF}{P_{in}}} \qquad \textbf{(2.3)}$$

2.4. External Quantum Efficiency (EQE)

The external quantum efficiency (EQE) or incident-photon-to-current efficiency (IPCE) is the ratio of the number of electrons collected (N_e) with the number of incident photons (N_p). It may be given as a function of wavelength or photon energy. As a function of wavelength (λ), the EQE (λ) is defined as the spectral response shown in **Equation 2.4.**

$$\boldsymbol{EQE(\lambda) = \frac{N_e}{N_p} = \frac{J_{SC}(\lambda)}{P_{in}(\lambda)} \cdot \frac{hc}{\lambda q} = \frac{J_{SC}(\lambda)}{P_{in}(\lambda)} \times \frac{1240}{\lambda}} \qquad \textbf{(2.4)}$$

where h is the Planck constant (6.62×10^{-34} J.s or 4.13×10^{-15} eV. s) and c is the speed of light in a vacuum (~$3\text{x}10^{8}$ m.s^{-1}). The EQE(λ) also can be calculated from $J_{SC}(\lambda)$ for the illuminated cell for each λ divided by the incident light intensity $P_{in}(\lambda)$. Thus, the integral of EQE(λ) over the entire λ gives the total photocurrent density (J_{SC}), defined in **Equation 2.5**.

$$\boldsymbol{J_{SC}^{EQE} = \int_{\lambda_{min}}^{\lambda_{max}} N_p(\lambda) \times EQE(\lambda) \times q \times d\lambda} \qquad \textbf{(2.5)}$$

where q is the magnitude of the electrical charge on the electron in C.

2.5. Resistances

Series resistance (R_S) and shunt resistance (R_{SH}) in photovoltaics are unavoidable parasitic parameters that influence the J-V characteristics of measuring solar cells. Their parameters determine how the current flows in a solar cell. Both R_S and R_{SH} can be modeled into an equivalent circuit model (**Figure 2.5**) to understand the energy loss mechanism. For the ideal solar cells, the photocurrent density J_P is simulated by a constant current source. The diode mainly controls the current flow in solar cells under applied bias and determines the J-V curve. However, the FF parameter from J-V can reach absolute 100% because the J-V curve cannot be rectangular. In reality, the parasitic resistances are unavoidable. Thus, the R_S and R_{SH} should be taken into account into the equivalent circuit for modeling the energy losses.[25]

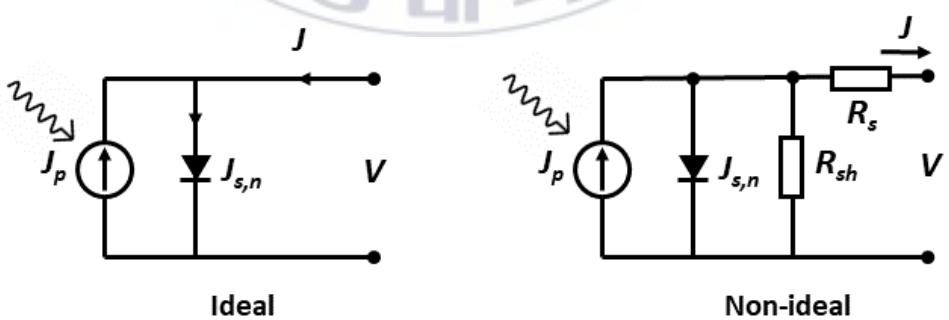

Figure 2.5 Ideal and non-ideal equivalent circuit of photovoltaic cells.

Commonly, the R_S is derived from the contact resistances between the photoactive layer and electrodes and the bulk resistances of the photoactive layer and electrodes. Meanwhile, the R_{SH} is derived from the current leakage in solar cells induced by pinholes or defect traps. The small increase in R_S can reduce the FF and in the severe case, the J_{SC} also can be affected if the R_S is very high. The R_S value for the ideal solar cell is zero. The shunt resistance is originated from the current leakage induced by pinholes and traps. The low value of R_{SH} provides an alternate current path, thus the power loss occurs in solar cells. Ideally, the R_S should reach infinity, thus the current doesn't flow into through the R_{SH}. If the R_{SH} value is low, the current flows through it cannot be averted leading to a lower FF.[20]

Chapter 3 Experimental Details

3.1 Materials and Preparation

3.1.1 Materials

Polyethylenimine 80% ethoxylated (PEIE), zinc acetate dihydrate, potassium hydroxide, ethanol, methanol, chlorobenzene, and 1,8-diiodooctane (DIO) were purchased from Sigma-Aldrich. Stearic acid (Acros Organics), PTB7-th (1-materials) and $PC_{70}BM$ (Merck KGaA) were purchased commercially. All materials were used without further purification.

3.1.2 The preparation of ZnO nanoparticles, PEIE/m-PEIE, and PTB7-th:$PC_{70}BM$ solution

ZnO nanoparticles were synthesized by mixing 2.95 g of zinc acetate dihydrate ($Zn(CH_3COO)_2 \cdot 2H_2O$) with in 130 mL of methanol solution and stirred for 2 h. The 1.48 g of potassium hydroxide (KOH) was added to 70 mL methanol and was sonicated for 30 min. The KOH solution was added dropwise to the zinc acetate solution and stirring for 4 h at 80°C. The precipitated ZnO nanoparticles were washed two times using methanol and dissolved in Methoxyethanol with the concentration of 20 mg/mL

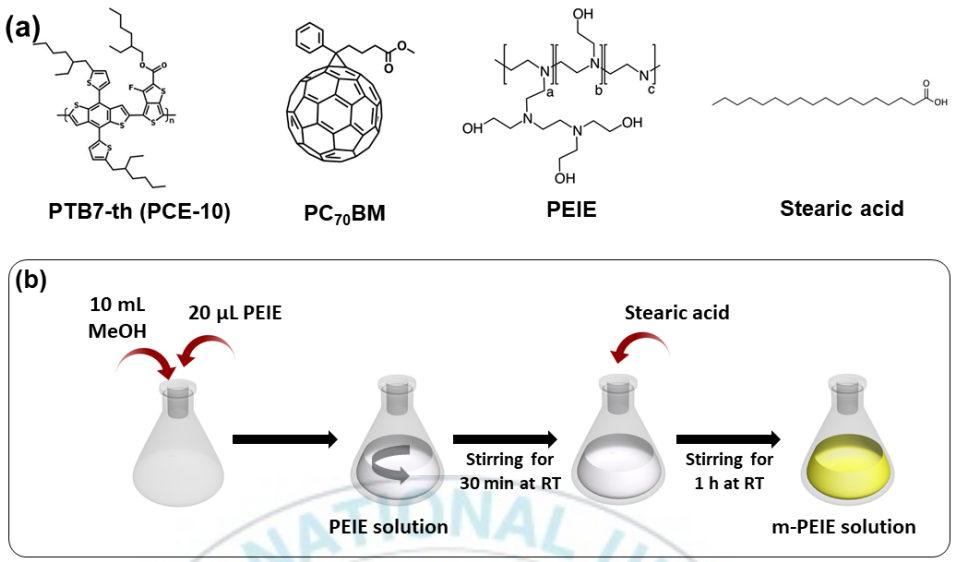

Figure 3.1 (a) The chemical structure of Polyethylenimine 80% ethoxylated and stearic acid, and (b) schematic illustration of the modification of PEIE solution using stearic acid.

Both PEIE and m-PEIE solutions were prepared by dissolving Polyethylenimine, 80% ethoxylated solution (20 mg) in ethanol (10 mL). For the m-PEIE solution, the stearic acid solution dissolved in methanol was added to obtain the m-PEIE solution and afterward stirred overnight. Both PEIE and m-PEIE solutions were filtered through a 0.5 polyvinylidene fluoride filter before use. The active layer solution was prepared by dissolving of PTB7-th (10 mg mL^{-1}) and $PC_{70}BM$ (18 mg mL^{-1}) in chlorobenzene (0.97 mL) and 1,8-diiodooctane (0.03 mL). The solution was

stirred overnight at 70 ^{o}C, then the solution was filtered using a 0.45 μm polytetrafluoroethylene filter. The chemical structures used in this study and the schematic of the modification of PEIE solution using stearic acid are shown in **Figure 3.1a, b.**

3.2 Fabrication of Organic Photovoltaic (OPV) Devices

The patterned ITO/glass substrates were sequentially cleaned with DI water, acetone and isopropanol for 10 min each. Meanwhile, the patterned ITO/PEN substrates were used without the cleaning process. The ITO substrates were treated with UV-ozone treatment for 1000 s and transferred to an Ar-filled glovebox. For the ultra-thin layer of PEIE and m-PEIE, 100 μl of PEIE or m-PEIE solution was spin-coated onto the ITO substrates at 2000 rpm for 60 s. These devices were dried at room temperature for 15 min. The active layer blend solution was spin-coated at 2000 rpm for 40 s and then dried for 3 h in Ar-filled glove box before metal deposition. The methanol treatment was done at 2000 rpm for 40 s to remove the DIO in the photoactive layer before metal deposition. Finally, MoO_x (6 nm) and Ag (100 nm) were thermally evaporated in a vacuum chamber (<4x10^{-6} Pa) through a metal shadow mask with an active area of

0.38 cm^2 defined by the overlap of cathode and anode. The schematic of a m-PEIE OPV device is shown in **Figure 3.2**.

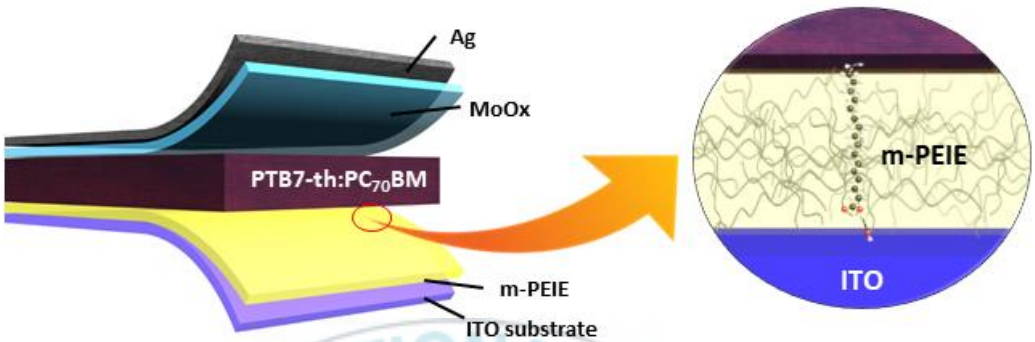

Figure 3.2 Scheme of a m-PEIE OPV device.

3.3 Measurements and Characterizations of OPV Devices

The current-voltage (J-V) curves were measured using a Keithley 2400A source unit under and calibrated AM 1.5G simulated illumination of 100 mW cm^{-2} in ambient air condition. The light intensity was calibrated using a standard Si-photodiode detector with a KG-5 filter (Newport Co., Oriel 91150V). External quantum efficiency (EQE) spectra were measured from a wavelength of 300 to 850 nm using the EQE measurement system (Newport Co., Oriel IQE-200™ system). The chopper frequency was set to 5 Hz to generate monochromatic light and a calibrated silicon photodiode was used as a reference. The optical transmittance spectra were obtained

using a UV-Vis spectrometer (Varian, Cary5000). The surface morphology of the cathode buffer layer films was observed by atomic force microscopy (Park system, Park NX10 AFM). The surface contact angle (wetting behaviour) was measured by a contact angle analyser (SEO, Phoenix-300). The work functions (WFs) of PEIE and m-PEIE layers were obtained by using ultraviolet photoelectron spectroscopy (UPS) (Thermo Scientific, Multilab-2000). The AC impedance spectroscopy was carried by using an impedance analyser compactstat electrochemical interface (IVIUM Technologies) in a frequency range of 1000 to 1 MHz and the applied bias voltage was set close to open circuit condition of the devices under AM 1.5G one sun illumination.

Chapter 4 Results and Discussion

4.1. Cathode Interfacial Layer (CIL) Analysis

4.1.1 Optical properties

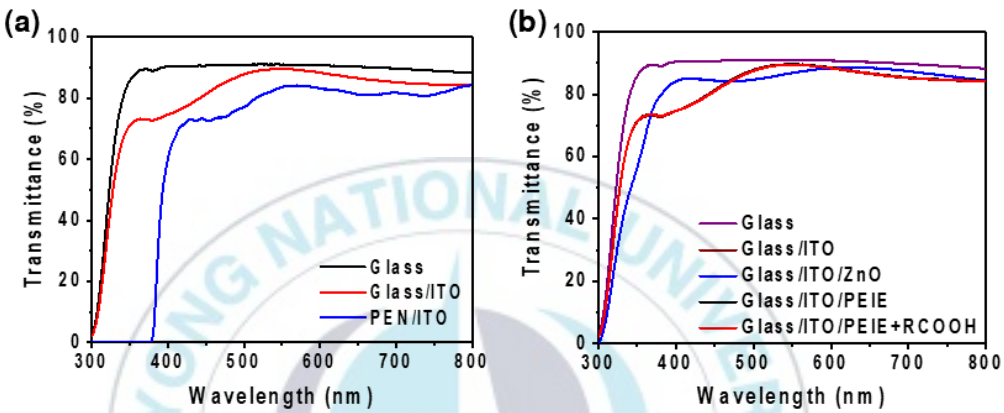

Figure 4.1 The transmittance spectra of (a) the glass, glass/ITO and PEN/ITO substrates, and (b) glass, glass/ITO, glass/ITO/PEIE and glass/ITO/m-PEIE.

The transmittance spectra of bare glass, ITO glass, and ITO PEN substrates are shown in **Figure 4.1a**. The ITO PEN shows the absence of the light transmittance in the ultraviolet region due to the naphthalene rings in the PEN main chain.[26] The transmittance spectra for PEIE and m-PEIE films on ITO glass substrates are shown in **Figure 4.1b**. Both PEIE and m-PEIE films have similar light transmittance. The ZnO on ITO glass has less

transmittance at the ultra-violet region due to its strong absorption at this region.

4.1.2 CIL layer properties: surface morphology, electrical, chemical and wetting characteristics

The atomic force microscopy (AFM) was used to investigate the surface properties of the CILs. As can be seen in the AFM images (**Figure 4.2a, b**), the m-PEIE film shows a smoother surface with a root-mean-square (rms) of 0.48 nm compared with PEIE with an rms of 0.75 nm. The smooth surface ensures the good electrical contact between the CIL and active layers, allowing better charge extraction.[27–30] Compared with m-PEIE, the PEIE film is relatively failing to uniformly make good contact with the photoactive layer.

Table 4.1. The average local photocurrent of PEIE and m-PEIE devices with respect to illumination intensities.

CILs	Dark	20W	40W	60W
PEIE	0.18	3.20	18.16	22.63
m-PEIE	4.66	13.3	26.25	27.3

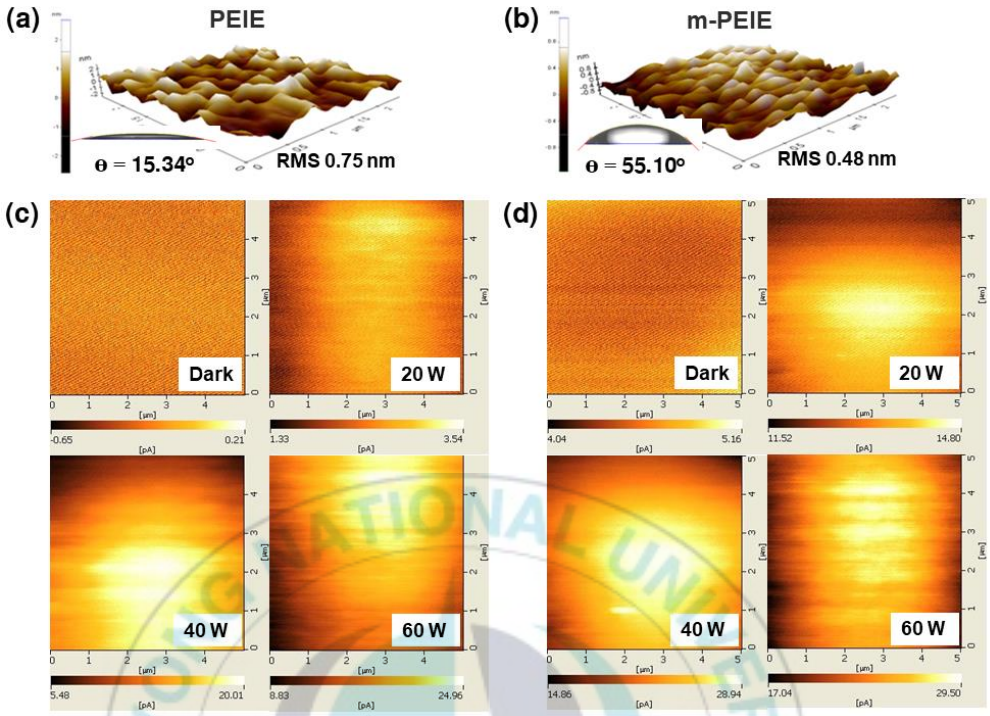

Figure 4.2 The atomic force microscopy (AFM) images of the (a) PEIE and (b) m-PEIE layers with contact angle images as inset figures. The photocurrent images of (c) PEIE and (d) m-PEIE with an applied bias to the substrate under different light intensity.

Photoconductive atomic force microscopy (pc-AFM) on the PEIE and m-PEIE CILs on the ITO glass substrates was also performed. The photocurrent was measured as a function of illumination intensity and the external bias of 3 V was applied to the sample during the measurement. The photocurrent mapping images with different illumination intensity is shown

in **Figure 4.2c,d**, and the average local photocurrent are summarized in **Table 4.1**. The m-PEIE CIL exhibits higher local photocurrents in every illumination compare to the PEIE CIL, allowing m-PEIE to tend more efficient charge extraction at the cathode interface.

To understand the wetting characteristic, we performed the contact angle with water as test media. The PEIE has a contact angle of 15.7^{o}. Meanwhile, the addition of stearic acid to PEIE leads to the improvement in hydrophobicity as shown in the contact angle image (**inset in Figure 4.2a,b**) and the contact angle H_2O on-PEIE surface with respect to stearic acid concentration is shown in **Figure 4.3**. The stearic acid addition to the PEIE increases the contact angle at 60 ppm concentration of stearic acid and becomes saturated beyond it. So, it can be assumed that the hydrophobic functional group of stearic acid covered the surface of PEIE layers. The hydrophobic surface improves the affinity of the m-PEIE with the photoactive layer spin-coated using hydrophobic chlorobenzene solvent.[31]

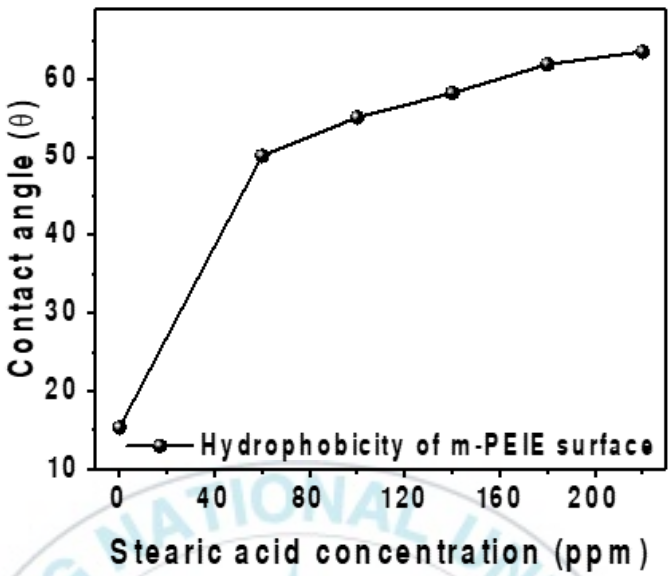

Figure 4.3 The contact angle of DI water on m-PEIE surface on ITO glass substrates with respect to stearic acid concentration.

To support the reason for hydrophobic behaviour, the modification of PEIE by the stearic acid was analyzed by Fourier transform infrared spectroscopy (FTIR). The FTIR spectra in the region from 4000 to 500 cm^{-1} are shown in **Figure 4.4**. For all samples, the peaks at 1047 and 1460 cm^{-1} are attributed to C-N and C-O bonds, respectively. The observed carboxylic group (C=O) in m-PEIE at 1705 cm^{-1} are attributed to –COOH in stearic acid. The N-H stretch and O-H stretch share peaks at a range of 3200 to 3500 cm^{-1}. An increase of peak intensity at 2938 cm^{-1} is attributed to the C-H stretch of stearic acid. The peak intensity of O-H stretch for m-PEIE is

observed decreases which indicating a decrease in the amount of OH hydrophilic sites. These hydrophilic sites of PEIE react with OH groups in stearic acid. These results suggest that the successful incorporation of stearic acid into PEIE.

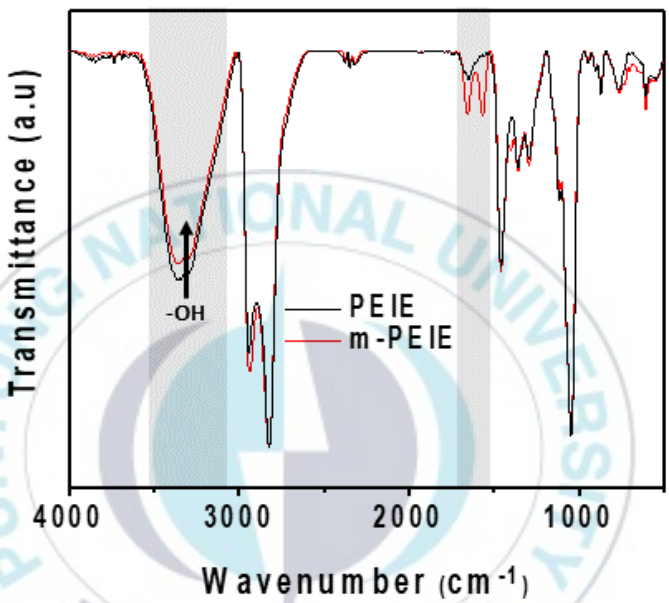

Figure. 4.4 The Fourier transform infrared spectroscopy (FTIR) spectra of PEIE and m-PEIE layers.

The work functions (WFs) of the PEIE and m-PEIE film spin-coated on ITO were estimated from the onsets of the secondary cut-off region ($E_{cut-off}$). As shown in ultraviolet photoelectron spectroscopy (UPS) results in **Figure 4.5**, the WF of PEIE is shifted from 4.4 to 4.1 via modification with stearic acid. The induced surface dipoles at the photoactive layer/cathode

interface is lowering the electrostatic potential at the interface, thus the WF become shifted. On account of the contact angle result, it is suggested that most of hydrophobic chains of stearic acid is located on the surface of m-PEIE. While the hydrophilic hydroxyl chain is located on the opposite direction, as a result the induced surface dipole further increased.

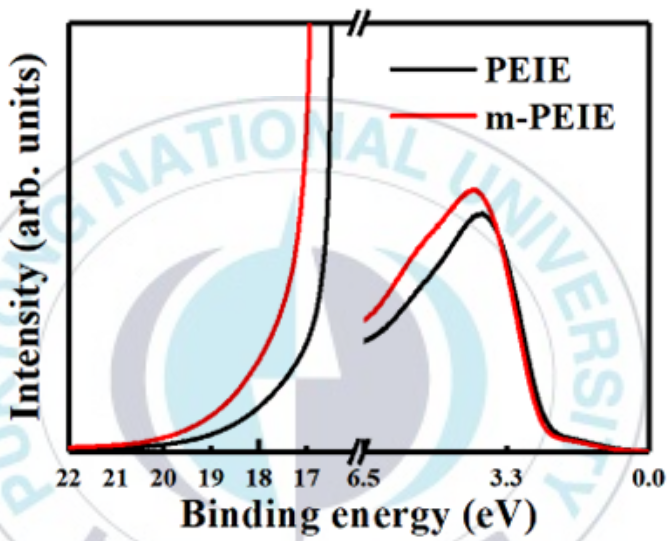

Figure. 4.5 Ultraviolet photoelectron spectroscopy (UPS) spectra of PEIE and m-PEIE on ITO substrates.

4.2 Characterizations and Measurement of OPV Devices

4.2.1 The incorporation of stearic acid on photovoltaic performance

In order to obtain the optimum condition of the addition of stearic acid to PEIE, we fabricated devices with different stearic acid concentration. The photovoltaic properties of the OPV devices with different stearic acid concentration is tabulated in **Table 4.2**. The device with the stearic acid concentration of 100 ppm shows the best efficiency compared to the others. Meanwhile, the stearic acid coated on the PEIE surface shows poor efficiency due to its low FF and J_{SC}.

Table 4.2 The photovoltaic properties of the PTB7-th:$PC_{70}BM$ with various concentration of stearic acid in PEIE.

Device	PCE best (%)	FF	V_{oc} (V)	J_{sc} (mA cm^{-2})	R_s (Ω)
PEIE	8.43	0.62	0.77	18.09	36.44
PEIE + 2 $mg.mL^{-1}$ SA	7.19	0.59	0.80	15.16	-
m- PEIE (60 ppm SA)	9.70	0.67	0.78	18.49	28.36
m-PEIE (100 ppm SA)	9.84	0.67	0.79	18.72	28.46
m-PEIE (140 ppm SA)	9.75	0.67	0.78	18.71	30.30
m-PEIE (180 ppm SA)	9.72	0.68	0.78	18.43	27.26
m-PEIE (220 ppm SA)	9.62	0.67	0.78	18.46	33.1

The J-V curve and external quantum efficiency (EQE) or the incident photon-to-current efficiency (IPCE) of the rigid OPVs with different CILs are respectively shown in **Figure 4.6a and 4.6b**, and the photovoltaic properties and calculated J_{SC} from the EQE measurement of these devices are summarized in **Table 4.3**.

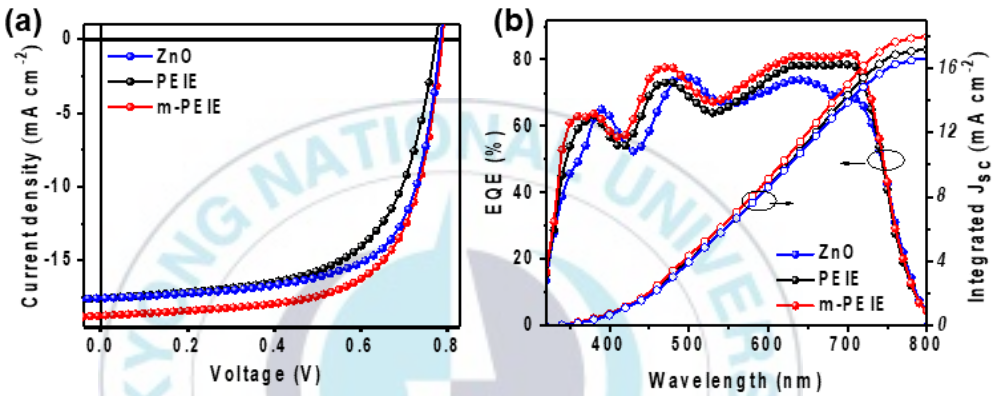

Figure. 4.6 (a) J-V and (b) EQE curve of PTB7-th:$PC_{70}BM$ rigid OPV devices on ITO glass substrates.

Table 4.3. The photovoltaic properties of the PTB7-th:$PC_{70}BM$ rigid OPV devices with PEIE and m-PEIE CILs.

Device	PCE best (%)	FF	V_{OC} (V)	J_{SC} (mA cm^{-2})	R_S	Calculated J_{SC} (mA cm^{-2})
ZnO	9.02	0.66	0.78	17.48	28.97	16.78
PEIE	8.43	0.62	0.77	17.66	36.44	17.24
m-PEIE	9.84	0.67	0.79	18.78	28.46	18.05

A PCE of 8.43%, a V_{OC} of 0.77 V, J_{SC} of 17.66 mA cm$^{-2,}$ and a FF of 0.62 is obtained by PEIE device. In contrast, the m-PEIE device as the best device achieved a PCE of 9.84% with a V_{OC} of 0.79 V, J_{SC} of mA cm$^{-2,}$ and a FF of 0.67. The improved J_{SC} of the m-PEIE device is originated from an increase of EQE value over the visible region compared to the PEIE device. The ZnO device was also measured for comparison. The ZnO device achieved the PCE of 9.02% (a V_{OC} of 0.78 V, J_{SC} of 17.47 mA cm$^{-2,}$ and a FF of 0.66). The measured J_{SC} from the J-V curve and the calculated J_{SC} from EQE value (integrated J_{SC}) obtained under AM 1.5G one sun illumination is in good agreement with the mismatch is less than 5%.

4.2.2 Recombination and Energy Loss in the Rigid OPV Devices

The V_{OC} or J_{SC} as a function of light intensity, electrochemical impedance spectroscopy (EIS), and dark J-V of rigid OPV devices were carried out to elucidate the charge recombination kinetics in OPV devices. First, the J-V measurement as a function of light intensity was performed to further investigate the charge recombination.

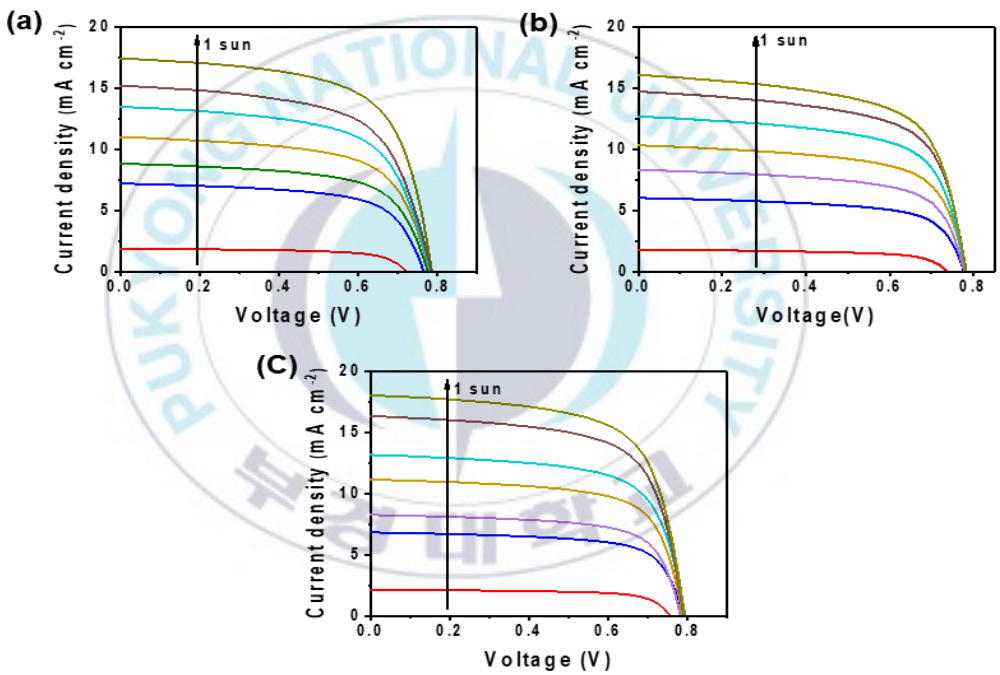

Fig. 4.7 J-V curves of devices (a) ZnO, (b) PEIE, and (c) m-PEIE OPV devices with respect to light intensity.

The J-V curves with respect to the light intensity for OPV devices are shown in **Figure 4.7a and 4.7b**, respectively. **Figure 4.8a** shows the J_{SC} as a function of the light intensity with a power-law relationship of $J_{SC} \propto I^{\alpha}$. The α value is an exponential factor that indicates bimolecular recombination and I is the light intensity. The device with the m-PEIE as a CIL shows an α of 0.95 which higher than those of PEIE-based (0.92) and ZnO (0.94). The α value of m-PEIE closes to unity (α=1) indicates reduced bimolecular recombination of carriers at 0 V. Moreover, the V_{OC} as a function of the light intensity was also investigated using **Equation 4.1**:

$$\boldsymbol{Voc(P) = \frac{nkT}{q}\ln(P) + C} \qquad \textbf{(4.1)}$$

where *k*, *T*, and *q* are the Boltzmann constant, the temperature, and the elemental charge, respectively. Meanwhile, *n* and *C* respectively represent the ideality factor and a constant.[32,33] As shown in **Figure 4.8b**, the n value extracted from the slope analysis shows that the ZnO, PEIE and m-PEIE have a value of 1.43, 1.57, and 1.26 *k*T/*q*, respectively. These results indicate that the m-PEIE device is almost free from trap-assisted recombination, while PEIE still exhibits the recombination.[32,34,35] The lower

bimolecular recombination and practically free from trap-assisted is affected by the enhanced internal electric field and improved photoactive layer quality.[21,36]

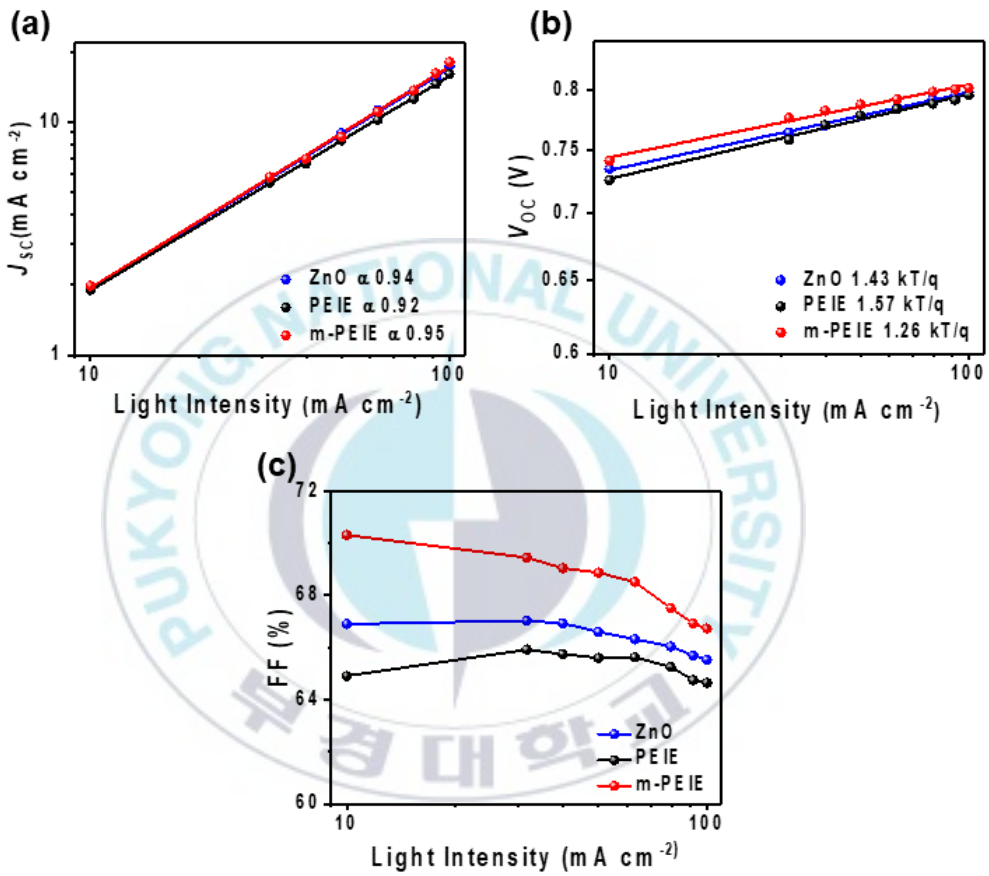

Figure 4.8 (a) The light-intensity dependence of J_{SC}, and (b) the light-intensity dependence of V_{OC}, (c) the light-intensity dependence of fill-factor of the OPV solar cells based on ZnO, PEIE and m-PEIE CILs.

Moreover, the m-PEIE device shows low-voltage loss at a low-light intensity which is beneficial for indoor low-light intensity applications.[21,36] The device with m-PEIE CIL has a large different FF value with the device with PEIE CIL at low light intensities. The light intensity dependence of the FF represents trap-assisted and bimolecular recombination in the OPV devices. As shown in **Figure 4.8c**, the PEIE device shows decrease under low light intensity indicating the trap-assisted recombination likely occurs. This behaviour might be linked to series resistance (R_S) and bimolecular recombination showing the capability of m-PEIE CIL to support charge transport.[37,38]

The internal resistance of the devices can be easily investigated by measuring the devices using electrochemical impedance spectroscopy (EIS) which shows as the semicircles in the Nyquist plot (**Figure 4.9**). The diameter of the semicircles indicates the charge transport resistance at the photoactive layer/cathode interface which at a glance shows that the m-PEIE device has lower recombination compare to PEIE devices.[39,40] To point out the Nyquist plot clearly, the data were fitted by using a simple parallel R-C equivalent circuit model comprising a resistor R_S and a resistor R_1 in series connection, and a capacitor C_1 in parallel connection. The

calculated R_S values for ZnO, PEIE and m-PEIE are 14.13, 19.97 and 13.75 Ω, respectively.[40,41] The lower value of R_S for m-PEIE devices can be attributed to the enhanced charge transport and indicates less recombination process at the photoactive layer/cathode interface.[39,42] Meanwhile, the PEIE device has high R_S value which indicated that there is a lot of accumulation of charges at the photoactive layer/cathode interface owing to the large energy level mismatch between the photoactive layer and ITO substrate.[24,35,43] These results reveal clearly that by employing the m-PEIE CIL could suppress the recombination at the photoactive layer/cathode interface where the photogenerated electron might be trapped. The charge transport and the bimolecular recombination can occur if there is a lot of electrons trapped at the photoactive layer/cathode interface, resulting in the high J_{SC} and FF.

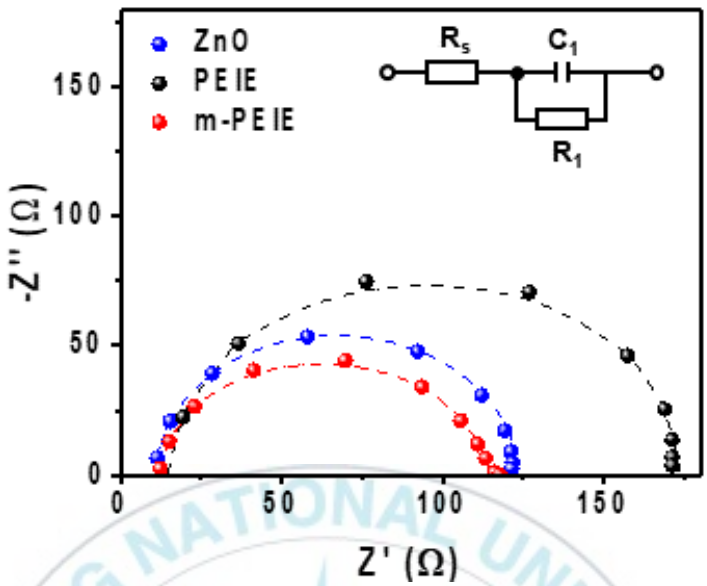

Figure 4.9 The electrochemical impedance spectroscopy (EIS) analysis.

The OPV devices were measured under dark conditions (**Figure 4.10a**) to gain deeper insights into the improved FF and J_{SC}. The shunt resistance plays an important role in controlling the leakage currents and indeed to FF and the series resistance influences the J_{SC}.[33,44] In the region -2 V to value close to 0.5 V, the leakage currents at the reverse bias of the m-PEIE device were remarkably suppressed compared to the PEIE device. Meanwhile, in the region over 1 V, the improved injection currents were noticed from the m-PEIE device indicating the improvement of the electron extraction into

the cathode electrode.[45] In opposite, the PEIE shows poor injection current compare to m-PEIE devices.

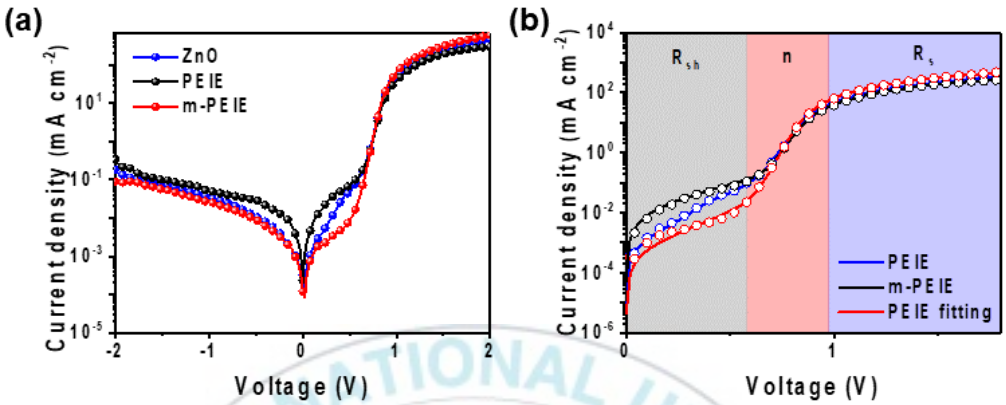

Figure 4.10 Semi-log dark J-V (a) curve and (b) dark J-V analysis and fitting of the OPV solar cells based on PEIE and m-PEIE CILs.

To further investigate the recombination mechanism in OPV devices, we also calculate the ideality factor (*n*). The ideality factor can represent the charge recombination in OPV due to traps or defects. In this study, the ideality factor was calculated by fitting from the slope in the exponential region in the dark J-V curve, as shown in **Figure 4.10b** by using

$$n = \frac{q}{k_B T} \frac{dV_{applied}}{d \ln J_{dark}} \quad \textbf{(4.2)}$$

the **Equation 4.2**:

where the $V_{applied}$ is the applied bias and the J_{dark} is the current density in dark condition. The parameters extracted from the fitting of dark J-V are summarized in **Table 4.4**. The ZnO, PEIE and m-PEIE devices exhibit the ideality factor of 1.39, 1.42 and 1.27, respectively. The ideality factor close to unity (n=1) gives a meaning of less trap-assisted and bimolecular recombination.[46]

Table 4.4. Parameters extracted from the fitting of dark J-V.

CILs	**n**	**R_S (Ω cm^2)**	**R_{SH} (Ω cm^2)**
ZnO	1.39	0.86	2.95×10^5
PEIE	1.42	3.05	5.94×10^4
m-PEIE	1.27	1.82	5.35×10^5

The different on V_{OC} those of PEIE and m-PEIE devices was also necessary to be assessed by the energy loss mechanism. Assuming that energy loss (E_{loss}) is defined by the difference between the bandgap E_g and the actual open-circuit voltage (V_{OC}). The E_g value was obtained from plotting of EQE with Tauc plot from **Figure 4.11.**

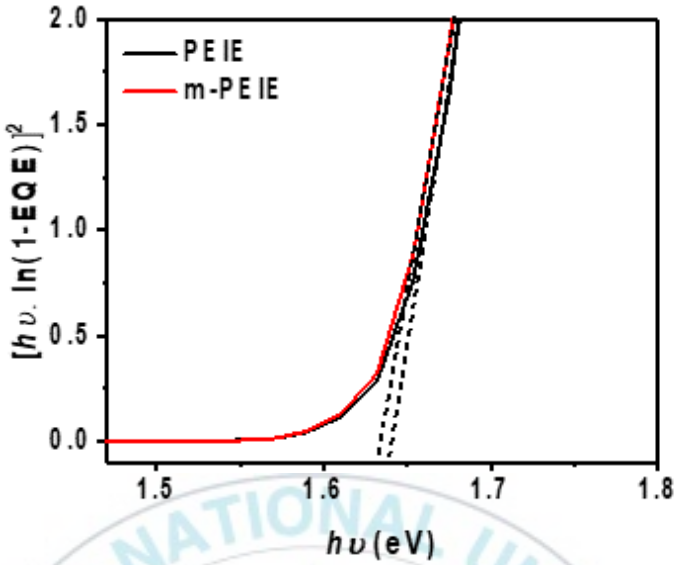

Fig. 4.11 [*hν ln*(1-EQE)]^2 vs *hν* curve of PEIE and m-PEIE with Tauc plot.

The energy loss in OPV devices is mainly originated from the charge recombination and the values is higher than 0.5 eV. The energy loss due to charge recombination is defined as E_{CT}-V_{OC}. An increase in the recombination will increase the E_{CT}-V_{OC}, thus lowering the V_{OC}.[47] The value is strongly affected by the saturation current which varies by orders of magnitude. The saturation current represents the recombination in the device and it strongly influences E_{CT}-V_{OC} as shown in the **Equation 4.3**:

$$\frac{E_{CT} - V_{oc}}{q} = \frac{k_B T}{q} \cdot \ln\left(\frac{J_{ph}}{J_0}\right) \quad \textbf{(4.3)}$$

where q, k_B, and T are elementary charge, the Boltzmann constant, and the temperature, respectively.[48] J_0 represents the saturation current of the diode extracted from the fitting of semi-log J-V curve.

Table 4.5. The values of the calculated energy loss

CILs	J_{SC} (mA cm^{-2})	J_0 (mA cm^{-2})	E_g (eV)	V_{OC} (meV)	E_{CT}-V_{OC} (meV)	Total E_{Loss} (meV)
PEIE	17.66	$5.17 \cdot 10^{-16}$	1.64	774	729.11	866
m-PEIE	18.78	$3.80 \cdot 10^{-16}$	1.63	787	707.32	843

As shown in **Table 4.5**, the m-PEIE exhibited a E_{CT}-V_{OC} value of ~707 meV which is lower compared to PEIE (~729 meV). The lower value of this energy loss indicating reduced the interfacial area for recombination in the m-PEIE devices. The low work function and the enhanced interfacial dipoles of the m-PEIE devices could improve the quality of electrical contact by forming Ohmic contact to fullerene acceptor.[49,50] The better photoactive layer morphology of the m-PEIE due to better affinity at the cathode/photoactive layer interface also aids the reduced the energy loss.[47,51] In contrast, the PEIE device may form the Ohmic contact to both fullerene acceptor and polymer donor. This condition will enhance the surface

recombination and leads to the reduction of the electric field, thus reducing the J_{SC} and V_{OC}.[49]

4.2.3 The photovoltaic performance, flexibility and air-storage stability of flexible OPV devices

To confirm the capability of the various CILs for the flexible OPVs, the flexible devices using an inverted structure with PTB7-th:$PC_{70}BM$ photoactive layer were fabricated. The flexible devices were measured under AM 1.5G one sun illumination (100 W cm^{-2}) and have not been attached to any glass substrates during measurement. **Figure 4.12a** shows the J-V curve of the various CILs and the photovoltaic properties are summarized in **Table 4.6**.

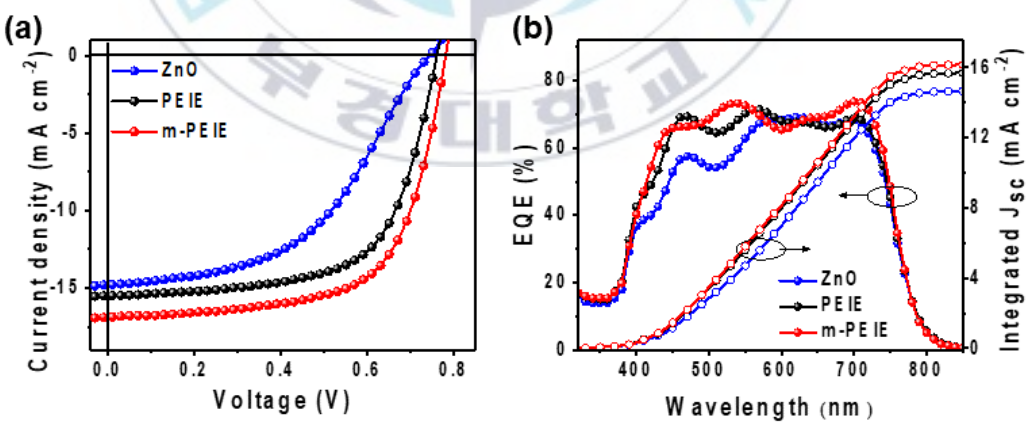

Figure 4.12 (a) J-V and (b) EQE curve of PTB7-th:$PC_{70}BM$ flexible OPV devices on ITO PEN substrates.

The m-PEIE flexible device achieved a PCE of 8.60% with a V_{OC} of 0.76 V, J_{SC} of 16.89 mA cm^{-2}, and a FF of 0.67 which is superior to those of PEIE flexible device with a PCE of 7.55% (a V_{OC} of 0.76 V, J_{SC} of 15.53 mA cm^{-2}, and a FF of 0.64). For comparison, the ZnO flexible device was also fabricated and measured. Different from the rigid OPV device, the PCE of ZnO flexible device shows lower efficiency even compare to PEIE device due to its 'S-shape' of J-V curve. The ZnO flexible device only achieved the best PCE of 5.32% (a V_{OC} of 0.76 V, J_{SC} of 15.53 mA cm^{-2}, and a FF of 0.64). The device statistics of OPV flexible devices with PEIE and m-PEIE CIL are shown in **Figure 4.13a-d**. The EQE spectra of flexible devices are shown in **Figure 4.12b**. The calculated J_{SC} value of the flexible devices are matching with the J_{SC} value obtained from J-V measurement with a mismatch is less than 5% which in acceptable error range. The flexible devices have low EQE value on the ultraviolet band due to the PEN substrates have less transmittance in this region.

Table 4.6. The photovoltaic properties of the of the PTB7-th:$PC_{70}BM$ flexible OPV devices on ITO PEN substrates.

Device	PCE (%)	FF	V_{OC} (V)	J_{SC} (mA cm^{-2})	R_S	Calc. J_{SC} (mA cm^{-2})
ZnO	5.32 (5.09±0.25)	0.54 (0.54±0.01)	0.46 (0.46±0.02)	14.96 (14.86±0.20)	58.20	14.80
PEIE	7.55 (7.59±0.12)	0.64 (0.64±0.01)	0.76 (0.76±0.01)	15.53 (15.65±0.40)	18.55	15.84
m-PEIE	8.44 (8.39±0.05)	0.66 (0.65±0.01)	0.78 (0.77±0.01)	16.66 (16.65±0.07)	15.82	16.33

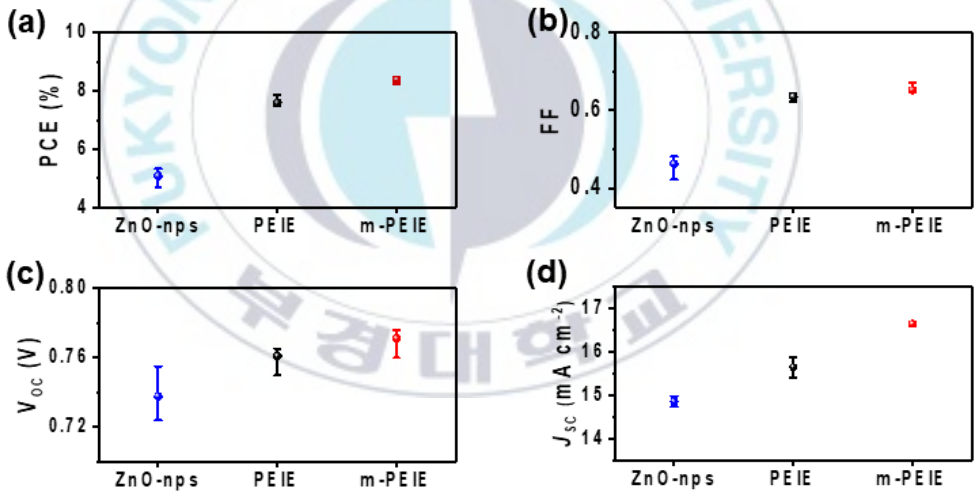

Figure 4.13 Device statistics of (a) PCE, (b) FF, (c) V_{OC}, and (d) J_{SC} for PEIE and m-PEIE OPV devices.

The bending test was employed to study the mechanical capability of the flexible OPVs with ZnO, PEIE and m-PEIE CILs. The devices were bent up to 200 bending cycles with different bending radius. As shown in **Figure 4.14**, there is no significant difference for PEIE and m-PEIE devices after they were bent with a radius of 1 cm. However, the PEIE device only can maintain 82% after it was bent with a radius of 0.55 cm. In contrast, the m-PEIE device maintained 95.8% after the bending test in the same condition. For comparison, we also check the bending test for the ZnO device. The PCE of the ZnO device drastically decreased after it was bent for 200 cycles with a radius of 0.75 cm.

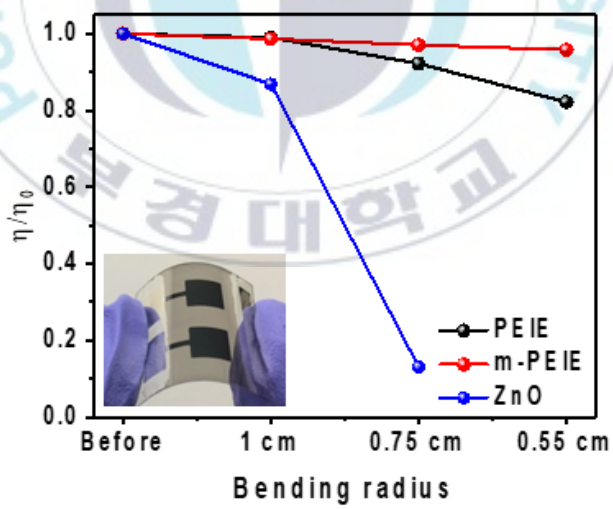

Figure 4.14 Proportional power conversion efficiency with respect to bending radius.

These results are might be associated with an increase in sheet resistance due to the crack on the ITO substrate and the delamination of the photoactive layer/ITO.[45,52] As shown in **Figure 4.15**, the ZnO ETL shows more numerous cracks compared to PEIE and m-PEIE CILs. It also revealed that a decrease in proportional efficiency of PEIE after it was bent at radius 0.75 to 0.55 cm might be associated to the delamination of the photoactive layer/ITO rather than the surface crack due to its less interface affinity.

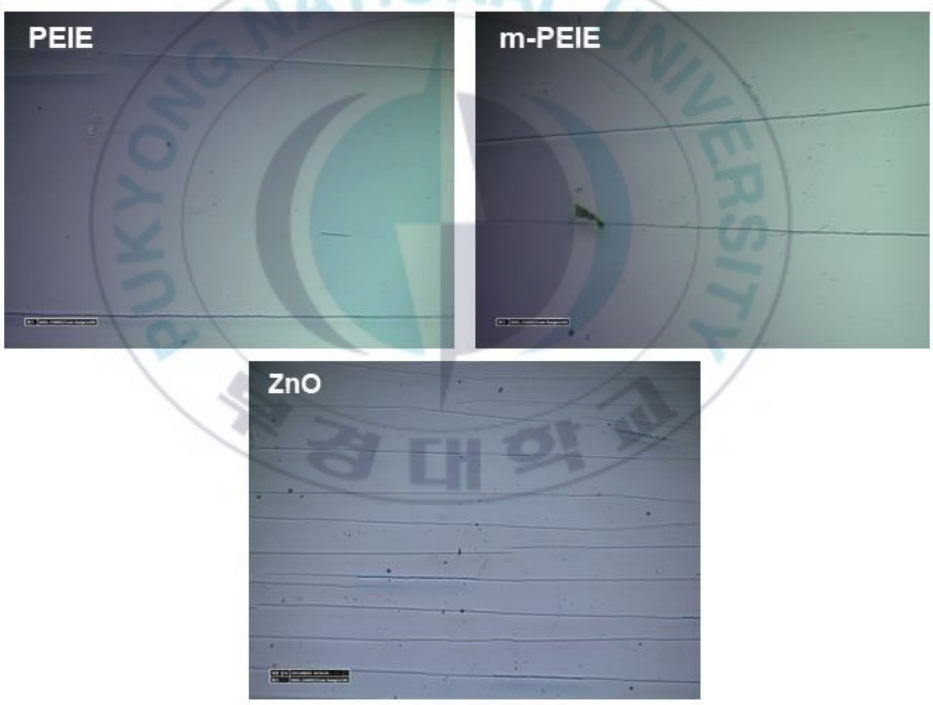

Figure 4.15 The optical microscope images of PEIE, m-PEIE and ZnO on PEN ITO after they were bent for 200 bending cycles at radius of 0.75 cm.

Additionally, the long-term air-storage stability of flexible OPV devices with various CILs was examined without any encapsulation process. The devices were measured every day under AM 1.5G on sun illumination in the ambient air condition. As shown in **Figure 4.16**, the m-PEIE device exhibits better stability compared to the PEIE device. The PCE of the m-PEIE device was retained 87.75% of initial performance after it was stored at ambient condition for 10 days. Meanwhile, the PCE of the PEIE device dropped down to 77.43% of the initial performance. The decrease in PCE is mainly influenced by a decrease in FF, rather than by V_{OC} and J_{SC}. This result suggests that the modification PEIE by the stearic acid hydrophobic molecule is efficacious to improve the air-storage stability of the devices by preventing moisture to penetrate the photoactive layer via its gap with the cathode. Moreover, the ZnO device can only maintained the proportional efficiency of 38.80% after it was aging for 10 days. The decrease in PCE of the ZnO device is influenced by a decrease in V_{OC}, J_{SC} and FF.

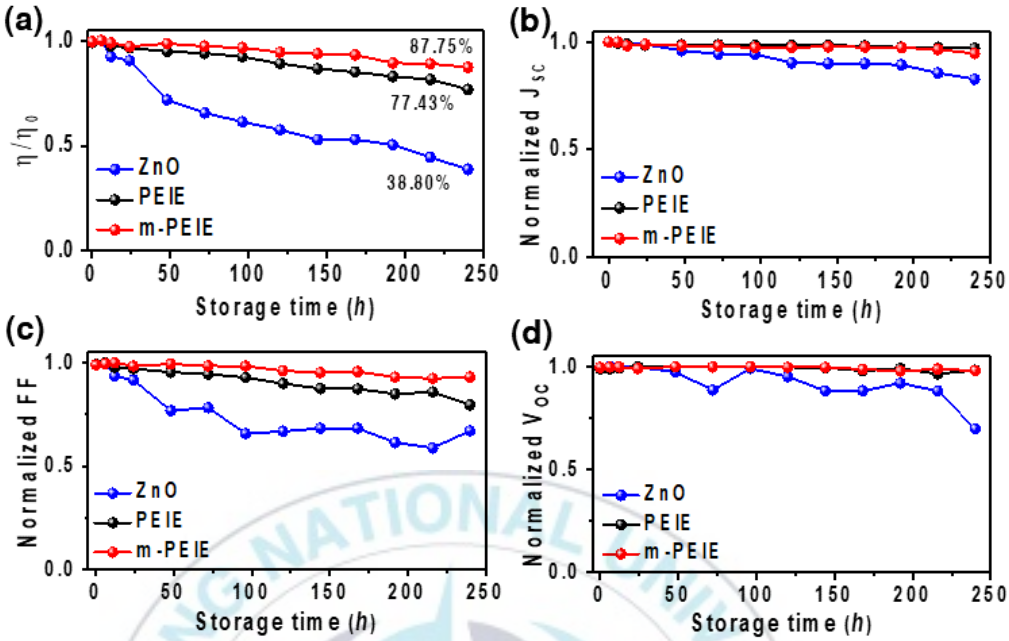

Figure 4.16 The device stability of (a) PCE, (b) J_{SC}, (c) FF, and (d) V_{OC} under ambient condition.

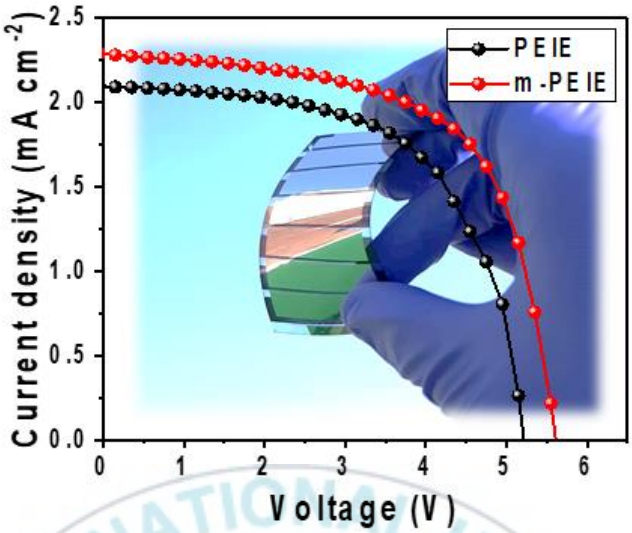

Figure 4.17 The J-V of OPV sub-modules with PEIE and m-PEIE CILs. The mini-module size is 5 x 7 cm^2 (7 cells, active area 13.16 cm^2).

For practical application, sub-module devices were fabricated on a 5 x 7 cm^2 size (7 cells) with an active area of 13.16 cm^2. The J-V curve is shown in **Figure 4.17** and the photovoltaic properties are summarized in **Table 4.7**.

Table 4.7. The photovoltaic properties of the PTB7-th:$PC_{70}BM$ sub-module OPV with PEIE and m-PEIE CILs

Device	PCE best (%)	FF	V_{OC} (V)	J_{SC} (mA cm^{-2})
PEIE	6.60	0.64	5.22	2.09
m-PEIE	7.97	0.63	5.47	2.31

The OPV module with m-PEIE CIL achieved a PCE of 7.97% (FF of 0.63, J_{SC} of 2.31 mA cm^{-2} and V_{OC} of 5.47 V) meanwhile the module with PEIE CIL only shows a PCE of 6.60% (FF of 0.64, J_{SC} of 2.09 mA cm^{-2} and V_{OC} of 5.22 V).

Conclusion

The rigid and flexible OPVs with a PCE of 9.87% and 8.60% were successfully fabricated using a room temperature process in an ambient condition realized by employing a hydrophobic stearic acid modified PEIE (m-PEIE) as CILs. The inclusion of stearic acid to PEIE not only improves the considerable charge extraction but also improves the mechanical and long-term air-storage stability. The improved charge transport is mainly attributed to a decrease on the recombination at the photoactive layer/cathode interface. The better WF alignment of m-PEIE to $PC_{70}BM$ also reinforces the improved device performance due to lower energy barrier. Moreover, a further improvement in the device was also expected to be supported by the improved photoactive layer quality due to good affinity with the hydrophobic surface of m-PEIE layer. The good affinity of photoactive/cathode interface also is expected can improve the mechanical stability during bending test due to it can prevent delamination. The hydrophobic nature of m-PEIE improved the long term air storage stability by preventing the moisture to penetrate the photoactive/cathode interface.

References

1. IEA, I. E. A. World Energy Outlook 2019 – Analysis - IEA. *World Energy Outlook 2019* (2019).

2. Luceño-Sánchez, J. A., Díez-Pascual, A. M. & Capilla, R. P. Materials for photovoltaics: State of art and recent developments. *International Journal of Molecular Sciences* **20**, 976 (2019).

3. NREL. Best Research-Cell Efficiency Chart | Photovoltaic Research | NREL. *Best Research-Cell Efficiency Chart | Photovoltaic Research | NREL* (2019).

4. Hofmann, A. I., Cloutet, E. & Hadziioannou, G. Materials for Transparent Electrodes: From Metal Oxides to Organic Alternatives. *Advanced Electronic Materials* **4**, 1700412 (2018).

5. Li, G., Zhu, R. & Yang, Y. Polymer solar cells. *Nature Photonics* **6**, 153–161 (2012).

6. MacDonald, W. A. *et al.* Latest advances in substrates for flexible electronics. *Journal of the Society for Information Display* **15**, 1075–1083 (2007).

7. Zhang, Z. *et al.* Non-conjugated polymers as thickness-insensitive electron transport materials in high-performance inverted organic solar cells. *Journal of Energy Chemistry* **47**, 196–202 (2020).

8. Zhou, Y. *et al.* A Universal Method to Produce Low-Work Function Electrodes for Organic Electronics. *Science* **336**, 327–332 (2012).

9. Xiong, S. *et al.* 12.5% Flexible Nonfullerene Solar Cells by Passivating the Chemical Interaction Between the Active Layer and Polymer Interfacial Layer. *Advanced Materials* **31**, 1806616 (2019).

10. Zhang, Y., Chen, L., Hu, X., Zhang, L. & Chen, Y. Low Work-function Poly(3,4-ethylenedioxylenethiophene): Poly(styrene sulfonate) as Electron-transport Layer for High-efficient and Stable Polymer Solar Cells. *Scientific Reports* **5**, 12839 (2015).

11. Yin, Z., Wei, J. & Zheng, Q. Interfacial Materials for Organic Solar Cells: Recent Advances and Perspectives. *Advanced Science* **3**, 1500362 (2016).

12. Li, P. *et al.* High-efficiency inverted polymer solar cells controlled by the thickness of polyethylenimine ethoxylated (PEIE) interfacial layers. *Physical Chemistry Chemical Physics* **16**, 23792–23799

(2014).

13. Yeo, J.-S. *et al.* In-depth considerations for better polyelectrolytes as interfacial materials in polymer solar cells. *Nano Energy* **21**, 26–38 (2016).

14. Huang, Y., Kramer, E. J., Heeger, A. J. & Bazan, G. C. Bulk Heterojunction Solar Cells: Morphology and Performance Relationships. *Chemical Reviews* **114**, 7006–7043 (2014).

15. Heeger, A. J. 25th Anniversary Article: Bulk Heterojunction Solar Cells: Understanding the Mechanism of Operation. *Advanced Materials* **26**, 10–28 (2014).

16. Rafique, S., Abdullah, S. M., Sulaiman, K. & Iwamoto, M. Fundamentals of bulk heterojunction organic solar cells: An overview of stability/degradation issues and strategies for improvement. *Renewable and Sustainable Energy Reviews* **84**, 43–53 (2018).

17. Hoppe, H. & Sariciftci, N. S. Morphology of polymer/fullerene bulk heterojunction solar cells. *Journal of Materials Chemistry* **16**, 45–61 (2006).

18. Aqoma, H. *et al.* 11% Organic Photovoltaic Devices Based on PTB7-

Th: PC71BM Photoactive Layers and Irradiation-Assisted ZnO Electron Transport Layers. *Advanced Science* **5**, 1700858 (2018).

19. Cui, Y. *et al.* Over 16% efficiency organic photovoltaic cells enabled by a chlorinated acceptor with increased open-circuit voltages. *Nature Communications* **10**, 2515 (2019).

20. Deibel, C. & Dyakonov, V. Polymer–fullerene bulk heterojunction solar cells. *Reports on Progress in Physics* **73**, 96401 (2010).

21. Cowan, S. R., Roy, A. & Heeger, A. J. Recombination in polymer-fullerene bulk heterojunction solar cells. *Physical Review B* **82**, 245207 (2010).

22. Kurpiers, J. *et al.* Probing the pathways of free charge generation in organic bulk heterojunction solar cells. *Nature Communications* **9**, 2038 (2018).

23. Cowan, S. R., Roy, A. & Heeger, A. J. Recombination in polymer-fullerene bulk heterojunction solar cells. *Physical Review B* **82**, 245207 (2010).

24. Lee, J.-H. *et al.* Reinforcing the Built-In Field for Efficient Charge Collection in Polymer Solar Cells. *Advanced Functional Materials* **28**,

1705079 (2018).

25. Qi, B. & Wang, J. Fill factor in organic solar cells. *Physical Chemistry Chemical Physics* **15**, 8972–8982 (2013).

26. Zardetto, V., Brown, T. M., Reale, A. & Di Carlo, A. Substrates for flexible electronics: A practical investigation on the electrical, film flexibility, optical, temperature, and solvent resistance properties. *Journal of Polymer Science Part B: Polymer Physics* **49**, 638–648 (2011).

27. Yu, H., Huang, X. & Huang, C. PEIE doped ZnO as a tunable cathode interlayer for efficient polymer solar cells. *Applied Surface Science* **470**, 318–330 (2019).

28. Ma, Z. *et al.* Influences of Surface Roughness of ZnO Electron Transport Layer on the Photovoltaic Performance of Organic Inverted Solar Cells. *The Journal of Physical Chemistry C* **116**, 24462–24468 (2012).

29. Wang, Z. *et al.* Urea-Doped ZnO Films as the Electron Transport Layer for High Efficiency Inverted Polymer Solar Cells. *Frontiers in chemistry* **6**, 398 (2018).

30. Xiao, B., Wu, H. & Cao, Y. Solution-processed cathode interfacial layer materials for high-efficiency polymer solar cells. *Materials Today* **18**, 385–394 (2015).

31. Azmi, R. *et al.* High-Efficiency Low-Temperature ZnO Based Perovskite Solar Cells Based on Highly Polar, Nonwetting Self-Assembled Molecular Layers. *Advanced Energy Materials* **8**, 1701683 (2018).

32. Kyaw, A. K. K. *et al.* Intensity Dependence of Current–Voltage Characteristics and Recombination in High-Efficiency Solution-Processed Small-Molecule Solar Cells. *ACS Nano* **7**, 4569–4577 (2013).

33. Proctor, C. M. & Nguyen, T.-Q. Effect of leakage current and shunt resistance on the light intensity dependence of organic solar cells. *Applied Physics Letters* **106**, 83301 (2015).

34. Proctor, C. M., Kuik, M. & Nguyen, T.-Q. Charge carrier recombination in organic solar cells. *Progress in Polymer Science* **38**, 1941–1960 (2013).

35. Wetzelaer, G.-J. A. H., Koster, L. J. A. & Blom, P. W. M.

Bimolecular and Trap-Assisted Recombination in Organic Bulk Heterojunction Solar Cells. *Organic Photovoltaics* 343–376 (2014) doi:doi:10.1002/9783527656912.ch11.

36. Cojocaru, L. *et al.* Determination of unique power conversion efficiency of solar cell showing hysteresis in the I-V curve under various light intensities. *Scientific Reports* **7**, 11790 (2017).

37. Sherkar, T. S., Momblona, C., Gil-Escrig, L., Bolink, H. J. & Koster, L. J. A. Improving Perovskite Solar Cells: Insights From a Validated Device Model. *Advanced Energy Materials* **7**, 1602432 (2017).

38. Jahandar, M. *et al.* High-Performance CH3NH3PbI3-Inverted Planar Perovskite Solar Cells with Fill Factor Over 83% via Excess Organic/Inorganic Halide. *ACS Applied Materials & Interfaces* **9**, 35871–35879 (2017).

39. Rasool, S. *et al.* Amine-Based Interfacial Engineering in Solution-Processed Organic and Perovskite Solar Cells. *ACS Applied Materials & Interfaces* **11**, 16785–16794 (2019).

40. von Hauff, E. Impedance Spectroscopy for Emerging Photovoltaics. *The Journal of Physical Chemistry C* **123**, 11329–11346 (2019).

41. Li, Z. *et al.* Impedance investigation of the highly efficient polymer solar cells with composite CuBr2/MoO3 hole transport layer. *Physical Chemistry Chemical Physics* **19**, 20839–20846 (2017).

42. Kim, S. *et al.* The role of cation and anion dopant incorporated into a ZnO electron transporting layer for polymer bulk heterojunction solar cells. *RSC Advances* **9**, (2019).

43. Sundqvist, A., Sandberg, O. J., Nyman, M., Smått, J.-H. & Österbacka, R. Origin of the S-Shaped JV Curve and the Light-Soaking Issue in Inverted Organic Solar Cells. *Advanced Energy Materials* **6**, 1502265 (2016).

44. Zhao, Y. *et al.* Enhanced charge collection in polymer photovoltaic cells by using an ethanol-soluble conjugated polyfluorene as cathode buffer layer. *Solar Energy Materials and Solar Cells* **93**, 604–608 (2009).

45. Hashemi, S. A., Ramakrishna, S. & Aberle, A. G. Recent progress in flexible–wearable solar cells for self-powered electronic devices. *Energy & Environmental Science* **13**, 685–743 (2020).

46. Kirchartz, T., Deledalle, F., Tuladhar, P. S., Durrant, J. R. & Nelson,

J. On the Differences between Dark and Light Ideality Factor in Polymer:Fullerene Solar Cells. *The Journal of Physical Chemistry Letters* **4**, 2371–2376 (2013).

47. Menke, S. M., Ran, N. A., Bazan, G. C. & Friend, R. H. Understanding Energy Loss in Organic Solar Cells: Toward a New Efficiency Regime. *Joule* **2**, 25–35 (2018).

48. Vandewal, K. *et al.* Increased Open-Circuit Voltage of Organic Solar Cells by Reduced Donor-Acceptor Interface Area. *Advanced Materials* **26**, 3839–3843 (2014).

49. Brabec, C. J. *et al.* Origin of the Open Circuit Voltage of Plastic Solar Cells. *Advanced Functional Materials* **11**, 374–380 (2001).

50. Mihailetchi, V. D., Blom, P. W. M., Hummelen, J. C. & Rispens, M. T. Cathode dependence of the open-circuit voltage of polymer:fullerene bulk heterojunction solar cells. *Journal of Applied Physics* **94**, 6849–6854 (2003).

51. Tang, Z. *et al.* Relating open-circuit voltage losses to the active layer morphology and contact selectivity in organic solar cells. *Journal of Materials Chemistry A* **6**, 12574–12581 (2018).

52. Li, Y., Xu, G., Cui, C. & Li, Y. Flexible and Semitransparent Organic Solar Cells. *Advanced Energy Materials* 1701791 (2018).